

Article

First-Principles Calculations of Interfacial Structure and Properties between WC Substrate and TiN Coating Based on Density Functional Theory

Mengchao Wang ¹ , Yan Liu ^{1,*}, Hui Chen ^{1,*}, Lijun Wang ¹ and Dengwen Hu ²

¹ Key Laboratory of Advanced Technologies of Materials, Ministry of Education, School of Materials Science and Engineering, Southwest Jiaotong University, Chengdu 610031, China; wangmengchao@my.swjtu.edu.cn (M.W.); lijun-123458@163.com (L.W.)

² Shanghai Key Laboratory of Materials Laser Processing and Modification, School of Materials Science and Engineering, Shanghai Jiao Tong University, Shanghai 200240, China; hudengwen@sjtu.edu.cn

* Correspondence: liuyanzt@163.com (Y.L.); xnrpt@swjtu.edu.cn (H.C.)

Abstract: The excellent adhesion strength between the substrate and coating in the field of cemented carbide-coated tools is the crux of ensuring the durability of coated tools. The TiN coating is often used as a bonding layer to improve the bonding strength between the substrate and outer coating. Insights into detailed information on the interfacial properties between substrate and coating are essential for developing coating structures with optimal adhesion properties. Therefore, first-principles calculations were used to investigate the anisotropy of the elastic characteristics of WC and TiN as well as the bonding mechanism at the interface. The findings demonstrate that WC and TiN bulks have different symmetries in their anisotropy of elastic characteristics. WC(0001) and TiN(111) slabs can be well-lattice matched thanks to the low lattice mismatch ratio (2.7%). The HCP stacking mode has larger bonding energy than the OT and hole stacking modes in the interface structure with identical terminating atoms. The C-HCP-Ti interface forms covalent and ionic bonds, which is thermodynamically stable ($\gamma = -1.127 \text{ J/m}^2$) and has the highest bonding strength ($W_{\text{ad}} = 8.899 \text{ J/m}^2$) among all interface structures. The results of this study provide a practical perspective for improving the mechanical properties of cemented carbide-coated tools.

Keywords: WC; TiN coating; interfacial structure; first-principles calculations; adhesion strength; electronic structure



Citation: Wang, M.; Liu, Y.; Chen, H.; Wang, L.; Hu, D. First-Principles Calculations of Interfacial Structure and Properties between WC Substrate and TiN Coating Based on Density Functional Theory. *Coatings* **2022**, *12*, 1076. <https://doi.org/10.3390/coatings12081076>

Academic Editor: Francisco J. G. Silva

Received: 4 July 2022

Accepted: 26 July 2022

Published: 30 July 2022

Publisher's Note: MDPI stays neutral with regard to jurisdictional claims in published maps and institutional affiliations.



Copyright: © 2022 by the authors. Licensee MDPI, Basel, Switzerland. This article is an open access article distributed under the terms and conditions of the Creative Commons Attribution (CC BY) license (<https://creativecommons.org/licenses/by/4.0/>).

1. Introduction

Cemented carbide is a powder metallurgy product that is widely utilized around the world [1]. Because of its adaptable combination of transverse fracture strength, hardness, toughness, and wear resistance, WC-Co cemented carbide is utilized extensively in many associated industries, including cutting tools for milling metal parts in the machining industry, wear components in molds, and drill parts in mining areas, etc. [2]. In the field of machining, these tools are known as the teeth of the industry, and WC-Co cemented carbide is often used as their substrate. However, these tools suffer from the challenges of strong friction, huge thermal shock, and high-temperature oxidation in the cutting area during the service process. It is difficult for a single cemented carbide material to meet the processing requirements of difficult-to-machine materials and high-speed cutting [3]. Although a modest number of additives (VC, Cr₃C₂, Mo₂C, NbC, TaC, etc., and their mixed additives) can be used to improve the mechanical characteristics [4,5], the hard coating is still an irreplaceable method to enhance the comprehensive performance of tools. As a result, almost all tool surfaces in current machining applications are prepared with commercial hard coatings by CVD or PVD [6].

TiN, a binary nitride of transition metal, is still frequently employed as a protective hard coating for bearing, cutting, and forming tools due to its low cost, superior abrasion

resistance, and corrosion resistance [7]. TiN coating on tools can improve the product's surface quality and extend the tool's service life. The golden yellow color of the TiN coating makes it useful as a tool wear indication. However, TiN coatings undergo severe oxidation at operating temperatures above 500 °C, resulting in coating failure [8]. Researchers have enhanced the cutting performance of TiN-based coatings by incorporating additional components (Al, Cr, Si, Y, etc.) into binary TiN coatings to create multi-component coatings (TiAlN [9], TiCrN [10], TiSiN [11], TiAlSiN [12], etc.) in order to fulfil the demanding processing requirements of difficult-to-machine materials. These multi-component coatings provide outstanding wear resistance, toughness, high-temperature oxidation resistance, and hardness characteristics. However, the addition of doping elements can cause lattice distortion in the crystal, which makes the coating have higher residual stress, resulting in poor film-substrate bonding. It is necessary to deposit a bonding layer between the multi-component coating and the substrate to improve the bonding force, among which TiN is one of the commonly used bonding layers [13]. In the research of many scholars, the application of the TiN contact layer significantly improves the film-substrate adhesion and cutting performance of the coating. According to Zhong et al., a rich WC(0001) and WC(10 $\bar{1}$ 0) cemented carbide substrate is advantageous for forming a coherent or semi-coherent interface between TiN and WC, enhancing the interface structure [14]. These characteristics improve the coating-substrate system's capacity to withstand damage from outside forces. As a result, commercial cemented carbide-coated tools, including CVD [15] and PVD [16] coatings, are frequently made with TiN serving as a bonding layer.

A good combination of the coating and the substrate is an important guarantee to improve the durability of the coating. The adhesion between the cemented carbide and coatings depends on WC-film bonding, film-substrate interlocking, and WC carbide embedment. Studies by Bouzakis et al. show that mechanical treatment of the substrate can significantly improve the machinability of the coating [17]. During the CVD coating process, the high-temperature increases the grain size of WC and reduces the residual compressive stress, which in turn leads to annealing and softening of the cemented carbide material. This softening reduces the cutting performance of CVD-coated carbide tools, resulting in high coating deformation and premature fatigue fracture. Skordaris et al. further proposed to improve the performance of the substrate based on the appropriate heat treatment technology to improve the cutting performance of the CVD coated tool [18]. These studies provide an explanation for the adhesion mechanisms between the cemented carbide and coatings in terms of the film-substrate interlocking and WC carbides embedment, while studies on WC–film bonding are lacking.

First-principles calculations are frequently employed in contemporary scientific research because they provide insight into interface structures at the atomic and electronic levels [19]. It is an important tool for in-depth explanation of some interface issues. Zhao et al. used first principles to reveal the interface structure and electronic characteristics of wear-resistant coating WC/TiC [20]. Zavodinsky et al. researched the adhesion in the TiN/ZrN layered systems by density functional theory (DFT) and pseudopotentials methods, which revealed that the interfacial structure greatly affects the adhesion of TiN/ZrN [21]. Rao et al. revealed the mechanism by which TiN-promoted graphitization transformation of diamond decreases the interface bond strength through TiN/diamond interface property calculations [22]. Through first-principles calculations, Fan et al. identified the bonding mechanism at the interface of TiC(111)/TiN(111) with various atomic stacking configurations [23]. All these studies have proved the importance of theoretical calculation in the study of interface structure. This method makes up for the lack of traditional experiments that lack atomic resolution.

Studying the interface characteristics and electrical structure of the film-based interface is important in order to fully utilize TiN film for the interface structure design of the coating in the tool application and improve the overall performance of the multi-component coating. Cemented carbides can be divided into about 20 types according to their microstructure and chemical composition. Among them, hexagonal WC occupies the most prominent

position in all hard phases of cemented carbide. More than 80% of all carbide grades contain WC, many of which are pure WC-Co alloys [1]. Co is distributed in the gaps of WC particles. The Co content of the cemented carbide used for cutting tools is low (≤ 12 wt.%), and the Co on the surface layer will be selectively etched away during the ion etching process prior to coating deposition [24]. Therefore, the interface bonding between cemented carbide and TiN film is mainly the bonding between WC and TiN. However, first-principles calculations of the WC/TiN interface have not been reported so far. The bonding strength between WC/TiN depends on their interfacial relationship. In this study, the structure and properties of the interface between WC and TiN were investigated by first principles, which could provide a theoretical basis for explaining their adhesion strength and stability.

2. Models and Computational Details

2.1. Bulk Unit Cell Structure Models

The contents of C and N affect the properties of WC and TiN. In the field of coated tools, WC and TiN satisfying the stoichiometric ratio showed better performance. Moreover, the close-packed hexagonal (hcp) WC phase has an extremely narrow range of homogeneity. In modern production lines, carbon can be controlled in the range of 0.05 wt% [1]. Therefore, a typical crystal model satisfying stoichiometry was selected in this study. In addition, considering the scale of the model and the computational power of the method, the stress and defect states introduced in the material production process are not considered in the modeling process. Figure 1 is a schematic diagram of the crystal used to construct the interface structure in the first-principles calculations. The bulk WC unit cell model with the hcp stacking form is shown in Figure 1a, which belongs to the P6-2m space group. Figure 1b depicts the Fm-3m space group's bulk TiN unit cell model with the face-centered cubic (fcc) stacking form. Geometric optimization of the WC and TiN unit cells is necessary to guarantee that the right unit cell structure is used during the computation procedure. The crystal atoms are relaxed but the original crystal structure is maintained during the geometric optimization process.

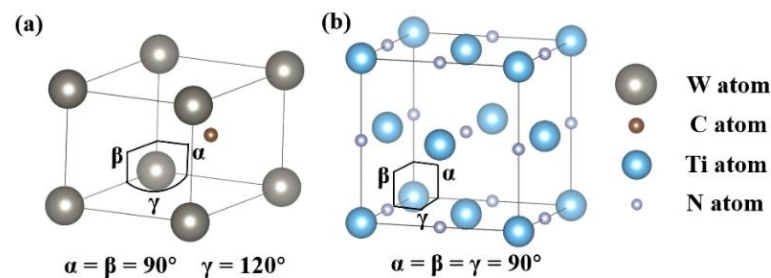


Figure 1. Crystal structures of (a) WC and (b) TiN (the colors of different atoms apply to the other models below).

2.2. Calculation Methods

The DFT-based Cambridge Serial Total Energy Package (CASTEP) was used to perform first-principles calculations on the bulk properties, interface structures, and electronic properties of WC and TiN. The interaction between ionic cores and valence electrons is described by the plane-wave ultrasoft pseudopotential approach [25]. The exchange-correlation function was described using the generalized gradient approximation (GGA) of Perdew–Burke–Ernzerh (PBE). Meanwhile, the Broyden–Fletcher–Goldfarb–Shannon (BFGS) algorithm was used to relax the atoms in order to minimize the system's overall energy and complete the geometry optimization [26]. The maximum force, maximum stress, maximum displacement, and convergence tolerances were specified at 0.01 eV/Å, 0.02GPa, 5.0×10^{-4} Å and 5.0×10^{-6} eV/atom, respectively. The normal state can be discovered by calculating the Kohn–Sham equation using the self-consistent-field (SCF) method with a convergence threshold of 5.0×10^{-7} eV/atom to carry out the electronic minimization. Plane wave expansion was measured at 350 eV with a kinetic energy cutoff

during convergence tests. For WC and TiN, the valence electrons considered are W-5s² 5p⁶ 5d⁴ 6s², C-2s² 2p², Ti-3s² 3p⁶ 3d² 4s², N-2s² 2p³. The Brillouin zone's irreducible edge was sampled using the regular Monkhorst–Pack grid, which has 10 × 10 × 10 points for WC bulk, 6 × 6 × 6 k points for TiN bulk, and 10 × 10 × 10 k points for slabs and interfaces. Surfaces and interfaces were modeled using the Supercell method with periodic boundary conditions. A supercell approximation method was used to construct slab and interface models with periodic boundary conditions. To prevent undesired interactions with the periodic crystalline structure, the surface and interface models set a 15 Å thick vacuum layer. The surface and interface models constructed in this study are pure and free of impurities. Models with adatom and vacancy defects will be addressed in further studies.

3. Results and Discussion

3.1. Bulk Property

3.1.1. Lattice Constant

To determine whether the chosen calculation parameters were realistic, the crystallographic parameters following unit cell optimization were compared to the experimental values of other scholars. The optimal lattice parameters for hcp-WC were $a = b = 2.92$ and $c = 2.84$ based on the geometric optimization, which agrees with the modified lattice parameters in [20]. The optimal lattice parameters for fcc-TiN were $a = b = c = 4.25$ Å, which agrees with the modified lattice parameters in [27]. It is clear that the computed results accord well with the other published references, proving that the simulation parameters set in this study were acceptable.

3.1.2. Property of WC Bulk

Figure 2 depicts the band structure and density of states (DOS) of WC bulk, where E_F stands for the Fermi level. In Figure 2a, an energy band spanning the Fermi level reveals that WC exhibits metallic characteristics. In Figure 2b, the W-d state dominates the total DOS (TDOS) at the Fermi level, showing that some metallic bonding exists in WC. This is consistent with the band structure's metallic characteristics (in Figure 2a). By examining the partial DOS (PDOS) of the C-p and W-d states, it can be shown that there is considerable orbital hybridization in the $-7.5 \sim -2.5$ eV and $2.5 \sim 10$ eV ranges, which suggests that WC has formed strong covalent bonds. The C-s state dominates the TDOS in the energy range of -14 to -10 eV, indicating that electrons are moved from the more electronegative W atoms to the more electronegative C atoms and form ionic bonds between them. As a result, hcp-WC bulk has a mixture of metallic, covalent, and ionic bonds, which is consistent with previous studies [20,25].

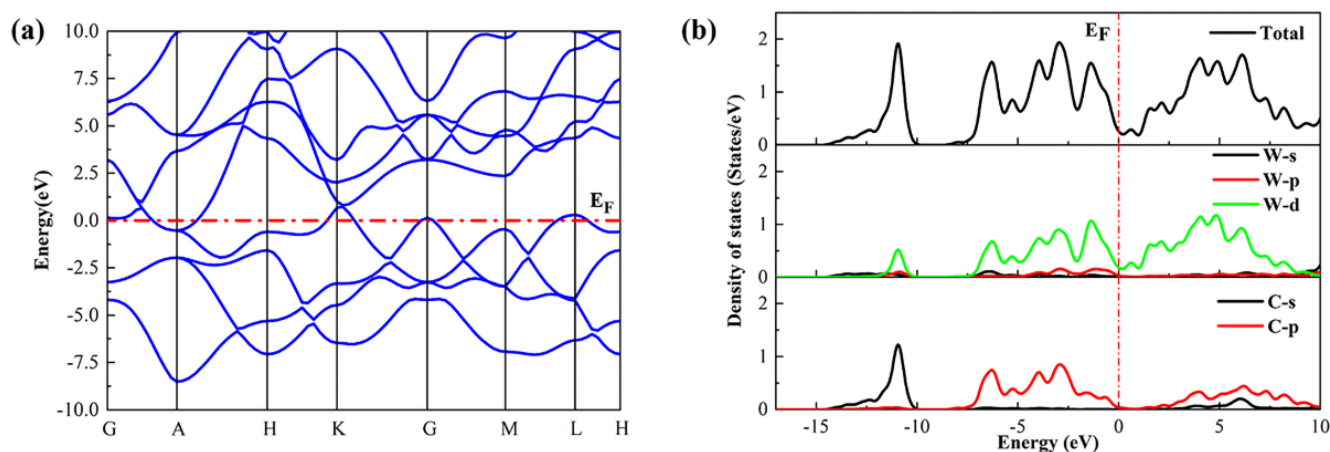


Figure 2. Calculated (a) band structure and (b) DOS of WC bulk.

Table 1 contains the computed elastic moduli of the WC bulk. Table 2 lists the Poisson's ratio, Young's modulus, shear modulus, and linear compressibility estimated by the ELATE of Gaillac et al. based on the elastic moduli in Table 1 [28]. The properties listed are anisotropic with unequal maximum and minimum values. Three-dimensional spherical maps and 2D projection maps (in Figure 3) on three orthogonal planes were both displayed using ELATE to more easily understand the anisotropy of the elastic characteristics of the WC bulk. In Figure 3, it can be clearly seen that the projection of all elastic properties on the xy plane presents a standard circle, indicating that there is no anisotropy in the xy plane. In the xz and yz planes, they have the same projected shape respectively and both present an ellipse or an irregular circle. Therefore, the anisotropy of the elastic properties of bulk WC is mainly contributed by the z-direction, and there is no anisotropy in the xy-direction. The asymmetric anisotropy feature of the WC bulk is related to the hcp crystal structure, which has only one sixfold symmetry axis in the z-axis direction [0001] [29].

Table 1. Elastic moduli of WC.

Direction	Total Elastic Moduli (GPa)					
	XX	YY	ZZ	XY	YZ	ZX
XX	714.02	209.97	159.85	0	0	0
YY	209.97	714.02	159.85	0	0	0
ZZ	159.85	159.85	947.2	0	0	0
XY	0	0	0	300.07	0	0
YZ	0	0	0	0	300.07	0
ZX	0	0	0	0	0	252.02

Table 2. Young's modulus, linear compressibility, shear modulus, and Poisson's ratio of WC.

WC	Young's Modulus GPa		Linear Compressibility TPa^{-1}		Shear Modulus GPa		Poisson's Ratio	
	E_{\min}	E_{\max}	β_{\min}	β_{\max}	G_{\min}	G_{\max}	ν_{\min}	ν_{\max}
Value	638.30	891.90	0.73	0.96	252.02	325.12	0.12	0.27
Anisotropy	1.397		1.303		1.290		2.151	

3.1.3. Property of TiN Bulk

Figure 4 depicts the band structure and DOS of TiN bulk, where E_F stands for the Fermi level. In Figure 4a, an energy band spanning the Fermi level reveals that TiN exhibits metallic characteristics. In Figure 4b, the Ti-d state dominates the TDOS at the Fermi level, indicating that TiN has some metallic bonding, which is consistent with the metallic properties exhibited in the band structure (in Figure 4a). Ti-d and N-p orbits have identical peak forms and peak amplitude in the energy range of -8.5 to -2.5 eV, indicating that there is orbital hybridization between the Ti and N atoms. This indicates the emergence of covalent bonds. Be-tween -17 eV and -14 eV, the Ti-d orbital interacts weakly with the N-s orbital. As can be seen, polar covalent bonds and metal bonds coexist in fcc-TiN bulk, which is in good accordance with earlier observations [27].

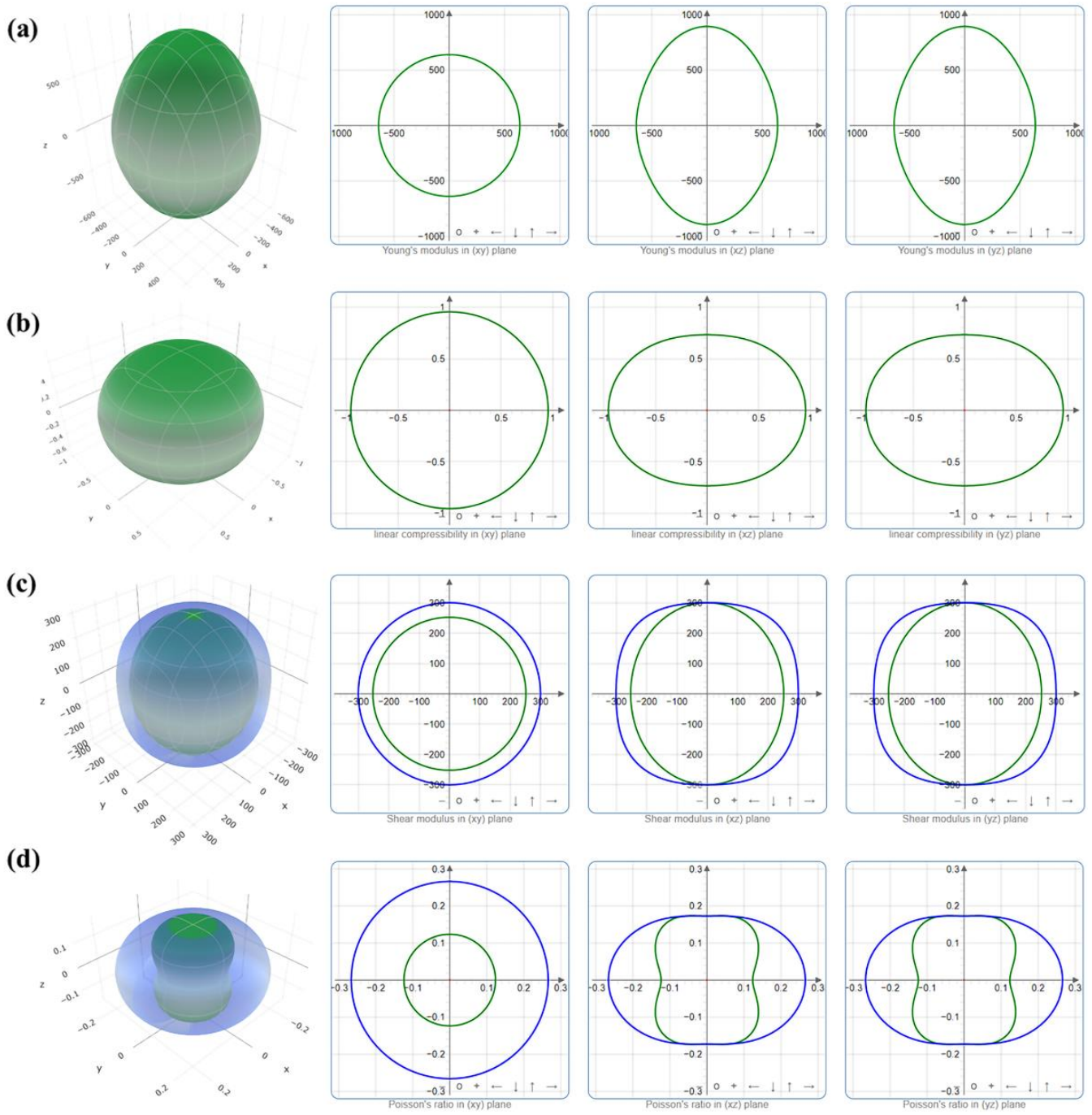


Figure 3. The 3D and 2D viewpoints of the WC bulk's (a) Young's modulus, (b) linear compressibility, (c) shear modulus, and (d) Poisson's ratio.

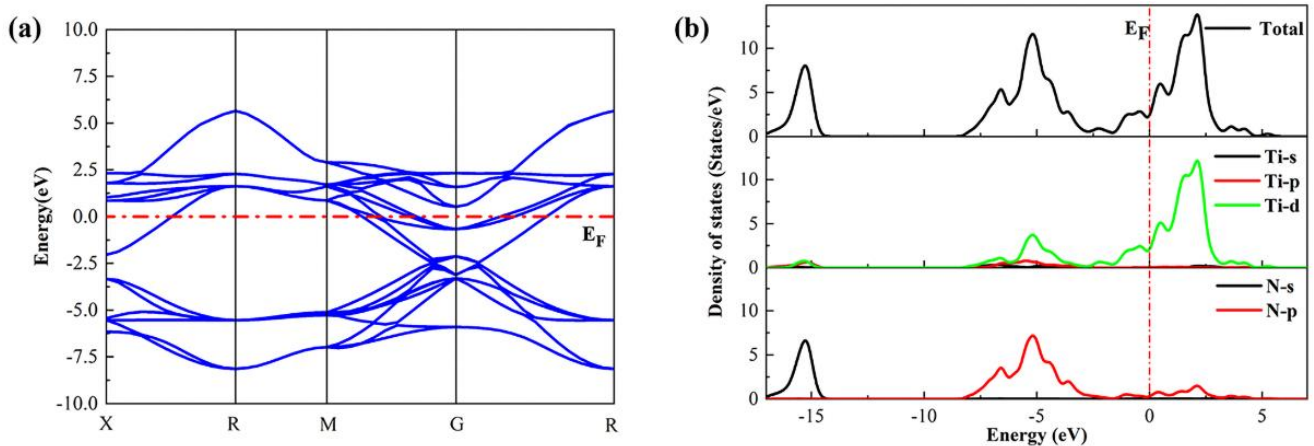


Figure 4. Calculated (a) band structure and (b) DOS of TiN.

Table 3 contains the computed elastic moduli of the TiN crystal. Table 4 lists the Poisson's ratio, Young's modulus, shear modulus, and linear compressibility estimated by the ELATE of Gaillac et al. based on the elastic moduli in Table 3 [28]. Except for linear compressibility, all other properties exhibit anisotropy. Three-dimensional spherical maps and 2D projection maps of the elastic characteristics of the TiN bulk on three orthogonal planes were both displayed in Figure 5. Figure 5a reveals that the Young's modulus has an anisotropy value of 1.485 and is the same in all three directions. There is no anisotropy if the 3D map is more spherical, indicating that the material is more isotropic [30]. In Figure 5b, the 3D map of linear compressibility is a very regular sphere; it is clear that the linear compressibility of TiN has no anisotropy, which corresponds to an anisotropy value of 1. The shear modulus of TiN exhibits the same anisotropy in the x , y , and z directions as does the Poisson's ratio, as shown in Figure 5c,d, with the corresponding anisotropy values of 1.414 and 2.770. As a result, we can conclude that the elastic properties of TiN bulk are strongly anisotropic with high symmetry. The mechanical properties of TiN are similar in specific symmetric crystal orientations. This symmetry is related to the high symmetry of the FCC structure, which has four threefold rotation axes oriented diagonally to the cube [111] [31].

Table 3. Elastic moduli of TiN.

Total Elastic Moduli (GPa)						
Direction	XX	YY	ZZ	XY	YZ	ZX
XX	630.71	96.17	96.17	0	0	0
YY	96.17	630.71	96.17	0	0	0
ZZ	96.17	96.17	630.71	0	0	0
XY	0	0	0	189.08	0	0
YZ	0	0	0	0	189.08	0
ZX	0	0	0	0	0	189.08

Table 4. Young's modulus, linear compressibility, shear modulus, and Poisson's ratio of TiN.

TiN	Young's Modulus GPa		Linear Compressibility TPa^{-1}		Shear Modulus GPa		Poisson's Ratio	
	E_{\min}	E_{\max}	β_{\min}	β_{\max}	G_{\min}	G_{\max}	ν_{\min}	ν_{\max}
Value	461.27	605.26	1.22	1.22	189.08	267.27	0.11	0.30
Anisotropy	1.312		1.000		1.414		2.770	

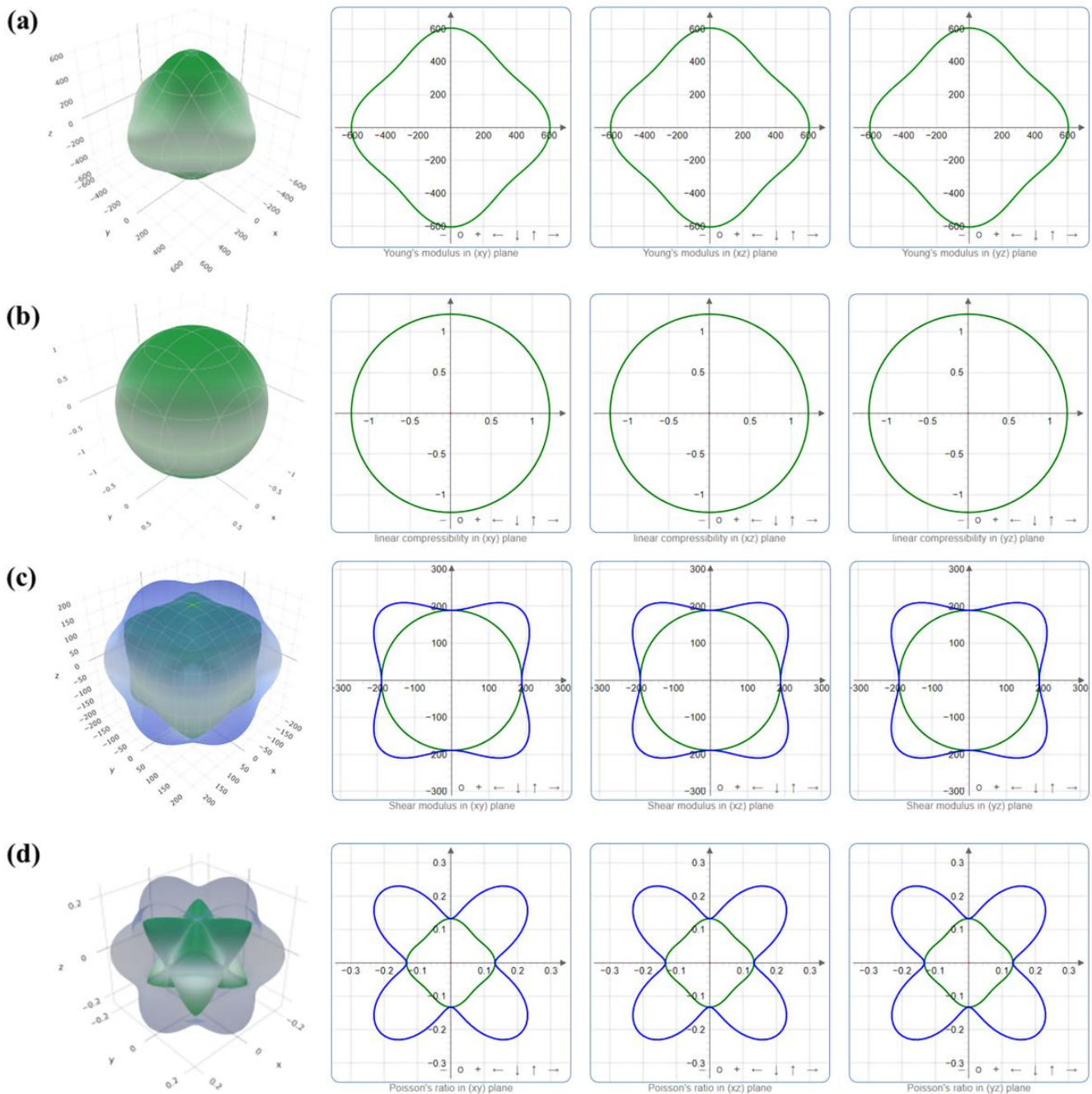


Figure 5. The 3D and 2D viewpoints of the TiN bulk’s (a) Young’s modulus, (b) linear compressibility, (c) shear modulus, and (d) Poisson’s ratio.

3.2. Lattice Mismatch between WC/TiN Interface

The WC/TiN interface’s lattice mismatch must be identified prior to interface construction. The lattice matching between the WC and TiN layers is improved by a lower lattice mismatch, which also improves interfacial adhesion and stability. The Bramfitt two-dimensional lattice mismatch theory was used to examine the lattice mismatch between the low index crystal faces of WC and TiN. The following is the two-dimensional lattice mismatch equation: [32]

$$\delta_{(hkl)_n}^{(hkl)_s} = \sum_{i=1}^3 \left[\left(\left| d_{[uvw]_s}^i \cos \theta - d_{[uvw]_n}^i \right| / d_{[uvw]_n}^i \right) / 3 \right] \times 100\% \tag{1}$$

where $(hkl)s$ is a lattice plane of WC substrate; $(hkl)n$ is a lattice plane of TiN coating; $[uvw]$ is the crystal orientation in (hkl) ; $d[uvw]$ is the interatomic spacing along $[uvw]$; θ is the angle between the $[uvw]s$ and $[uvw]n$.

Based on the above optimized crystal constant $a = b = 2.92 \text{ \AA}$, $c = 2.84 \text{ \AA}$ for hcp-WC, and $a = b = c = 4.25 \text{ \AA}$ for fcc-TiN, the lattice mismatch of WC/TiN interface is listed in Table 5. The lattice mismatch ratio of the WC(0001)/TiN(111) interface is only 2.7%, indicating that WC(0001)/TiN(111) has a good lattice matching. Therefore, in order to construct surface and interface models, the WC(0001) and TiN(111) lattice planes were chosen.

Table 5. Calculated lattice mismatch between WC and TiN.

Matching Face	WC(0001)//TiN(100)			WC(0001)//TiN(110)			WC(0001)//TiN(111)		
	$[11\bar{2}0]$	$[01\bar{1}0]$	$[\bar{1}2\bar{1}0]$	$[11\bar{2}0]$	$[01\bar{1}0]$	$[\bar{1}2\bar{1}0]$	$[11\bar{2}0]$	$[01\bar{1}0]$	$[\bar{1}2\bar{1}0]$
$[uvw]WC$	$[11\bar{2}0]$	$[01\bar{1}0]$	$[\bar{1}2\bar{1}0]$	$[11\bar{2}0]$	$[01\bar{1}0]$	$[\bar{1}2\bar{1}0]$	$[11\bar{2}0]$	$[01\bar{1}0]$	$[\bar{1}2\bar{1}0]$
$[uvw]TiN$	$[1\bar{1}0]$	$[2\bar{1}0]$	$[100]$	$[1\bar{1}1]$	$[1\bar{1}0]$	$[1\bar{1}1]$	$[101]$	$[11\bar{2}]$	$[01\bar{1}]$
θ ($^\circ$)	0	11.565	15	0	5.264	10.528	0	0	0
$dWC(\text{\AA})$	2.922	5.061	2.922	2.922	5.061	2.922	2.922	5.061	2.922
$dTiN(\text{\AA})$	2.123	4.747	3.003	3.677	6.006	3.677	3.003	5.201	3.003
δ (%)	16.04%			19.50%			2.70%		

3.3. Surface Convergence Test

Periodic boundary conditions serve as the foundation for surface and interface models. Convergence tests of the slabs were conducted prior to building the interface models to ascertain the minimal number of atomic layers required when the slabs resembled the internal structure of the bulk. The two terminal surfaces of all surface models must be terminated in the identical manner to eliminate the dipole effect. Figure 6 shows the surface models of WC(0001) and TiN(111). The WC(0001) slabs and TiN(111) slabs are both polar surfaces. There are two surface configurations of WC(0001) slab depending on the terminated atoms, which are (a) W-terminated and (b) C-terminated. However, TiN has six surface configurations, which are (c) Ti1-terminated, (d) Ti2-terminated, (e) Ti3-terminated, (f) N1-terminated, (g) N2-terminated, (h) N3-terminated.

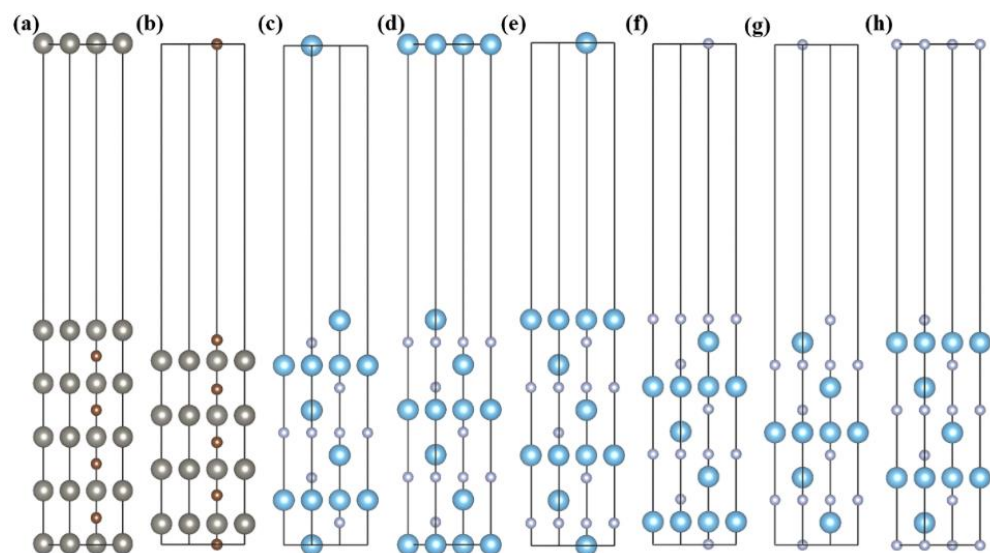


Figure 6. Surface models of (a) WC(0001) W-terminated; (b) WC(0001) C-terminated; (c) TiN(111) Ti1-terminated; (d) TiN(111) Ti2-terminated; (e) TiN(111) Ti3-terminated; (f) TiN(111) N1-terminated; (g) TiN(111) N2-terminated; (h) TiN(111) N3-terminated.

In this study, the variation in surface energy with atomic layer number is used to examine the number of atomic layers required to achieve bulk-like properties for the

surface model. Calculating the surface energy requires taking into account the chemical potentials of various elements due to the non-stoichiometric properties of the TiN(111) surface. Equation (2) can be used to compute the surface energy of the TiN(111) surface [33]:

$$\sigma_{TiN(111)}^{slab} = \frac{1}{2A_{sur(TiN(111))}} \left[E_{TiN(111)}^{slab} - N_{Ti}\mu_{Ti}^{slab} - N_N\mu_N^{slab} \right] \quad (2)$$

where $E_{TiN(111)}^{slab}$ is the total energy of fully relaxed TiN(111) surface; $A_{sur(TiN(111))}$ is the surface area of TiN(111) surface; μ_{Ti}^{slab} and μ_N^{slab} are the numbers of Ti, N atoms in the TiN(111) surface models; μ_{Ti}^{slab} and μ_N^{slab} represents the chemical potentials of Ti and N atoms.

The structure of TiN(111) surface will eventually gravitate toward an equilibrium state after complete relaxation, in which chemical potential of the surface is equal to that of the bulk. Consequently, different forms of energy are related in the ways listed below:

$$\mu_{TiN}^{bulk} = \mu_{Ti}^{slab} + \mu_N^{slab} \quad (3)$$

$$\Delta H_{TiN} = \mu_{TiN}^{bulk} - \mu_{Ti}^{bulk} - \mu_N^{bulk} \quad (4)$$

where μ_{TiN}^{bulk} is the total energy of TiN bulk; μ_{atom}^{bulk} is the total energy of the atoms in the corresponding pure phase (Ti and nitrogen); ΔH_{TiN} is the heat of formation of TiN bulk.

The surface energy in Equation (5) can be obtained by combining Equation (2) with Equation (3):

$$\sigma_{TiN(111)}^{slab} = \frac{1}{2A_{sur(TiN(111))}} \left[E_{TiN}^{slab} - N_N\mu_{TiN}^{bulk} - (N_{Ti} - N_N)\mu_{Ti}^{slab} \right] \quad (5)$$

Introduce a chemical potential change $\mu_{Ti} = \mu_{Ti}^{slab} - \mu_{Ti}^{bulk}$. Equation (5) becomes:

$$\sigma_{TiN(111)}^{slab} = \frac{1}{2A_{sur(TiN)}} \left[E_{TiN}^{slab} - N_N\mu_{TiN}^{bulk} - (N_{Ti} - N_N)\mu_{Ti}^{bulk} - (N_{Ti} - N_N)\Delta\mu_{Ti} \right] \quad (6)$$

where the numbers of atoms satisfies the formula $N_{Ti} = N_N + 1$ in the Ti-terminated TiN(111) surface and $N_{Ti} = N_N - 1$ in the N-terminated TiN(111) surface.

Furthermore, Ti and N atoms must also have smaller chemical potentials in the surface configuration than in the single phase; otherwise, the surface model will be unstable and will decompose into a more stable phase. Therefore, there are the following relationships:

$$\Delta\mu_N = \mu_N^{slab} - \mu_N^{bulk} \leq 0 \quad (7)$$

$$\Delta\mu_{Ti} = \mu_{Ti}^{slab} - \mu_{Ti}^{bulk} \leq 0 \quad (8)$$

Combined with Formulas (3), (4), (7) and (8), it can be seen that:

$$\Delta H_{TiN} = \mu_{Ti}^{slab} + \mu_N^{slab} - \mu_{Ti}^{bulk} - \mu_N^{bulk} = \Delta\mu_{Ti} + \Delta\mu_N \leq 0 \quad (9)$$

The range of values of $\Delta\mu_C$ can be given by the following equation:

$$\Delta H_{TiN} \leq \Delta\mu_{Ti} \leq 0 \quad (10)$$

As the same as TiN(111) surface configuration, WC(0001) surface configuration also does not conform to stoichiometric ratio and belongs to polar surface. Then the surface energy of WC(0001) calculated formula is:

$$\sigma_{WC(0001)}^{slab} = \frac{1}{2A_{sur(WC(0001))}} \left[E_{slab} - N_W\mu_{WC}^{bulk} + (N_W - N_C)\mu_C^{bulk} + (N_W - N_C)\Delta\mu_C \right] \quad (11)$$

$$\Delta H_{WC} \leq \Delta\mu_C \leq 0 \quad (12)$$

where the numbers of atoms satisfies the formula $N_W = N_C + 1$ in the WC(0001) W-terminated surface model and $N_W = N_C - 1$ in the WC(0001) C-terminated surface model.

According to Formulas (6), (10), (11), and (12), it can be seen that $(N_{Ti} - N_N)\Delta\mu_{Ti}$ and $(N_W - N_C)\Delta\mu_C$ is a constant given the values of $\Delta\mu_{Ti}$ and $\Delta\mu_C$. The chemical potentials of the corresponding atoms in the WC and TiN slabs were set equal to the chemical potential of the bulk to facilitate comparison of the trends of $\sigma_{TiN(111)}^{slab}$ and $\sigma_{WC(0001)}^{slab}$ with the number of layers and to determine the stability of the WC/TiN interface in subsequent studies.

Figure 7 depicts the surface energy of various atom-terminated types of WC(0001) and TiN(111) with increasing layer count. It should be pointed out that for the Ti/N-terminated face, according to the calculation results, the surfaces with the same terminating elements but different arrangements have the same surface energy. The surface energies of different surface models gradually tend to be constant with the number of atomic layers increases. When the number of layers of WC(0001) slabs is greater than or equal to nine, the surface energy of W-terminated slabs can be stabilized to about 3.50 J/m², and the surface energy of C-terminated slabs can be stabilized to about 5.60 J/m². With more than 11 layers of TiN(111) slabs, the surface energy of Ti-terminated slabs can be stabilized to about 1.80 J/m², and the surface energy of the N-terminated slabs can be stabilized to about 5.20 J/m². Considering the cost of the calculation process and ensuring the accuracy of the calculation results, a 9-layered WC(0001) W-terminated surface model, a 9-layered WC(0001) C-terminated surface model, an 11-layered TiN(111) Ti-terminated surface model, and an 11-layered TiN(111) N-terminated surface model were used to build the interface model.

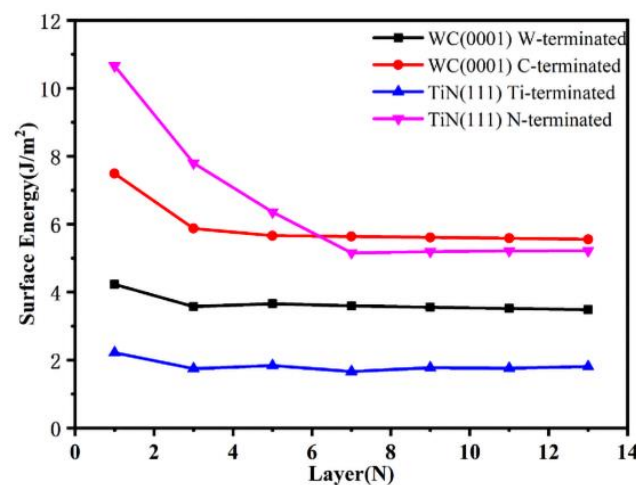


Figure 7. Variation of surface energy with the number of atomic layers for different terminated atomic surface models.

3.4. Interface Properties

3.4.1. Interface Structure

Considering the different stacking modes, a total of twelve interface structures were constructed. The schematic diagram of the structure of different interface models is shown in Figure 8. The top and bottom parts of the interface are not shown given the length of the schematic. The upper part is shown as a side view and the lower part is shown as a top view. Three possible stacking points are considered in the calculation. The twelve interfacial structures are named according to the corresponding situations of interfacial atoms. The OT denotes that the interfacial Ti/N atom of the TiN side is directly on top of the W/C atom in the WC side's surface. The hole denotes the Ti/N atom on the TiN side being placed on top of the vacancy on the WC side. The HCP denotes that the Ti/N atom of the TiN side is directly on top of the W/C atom in the second layer of the WC side [20].

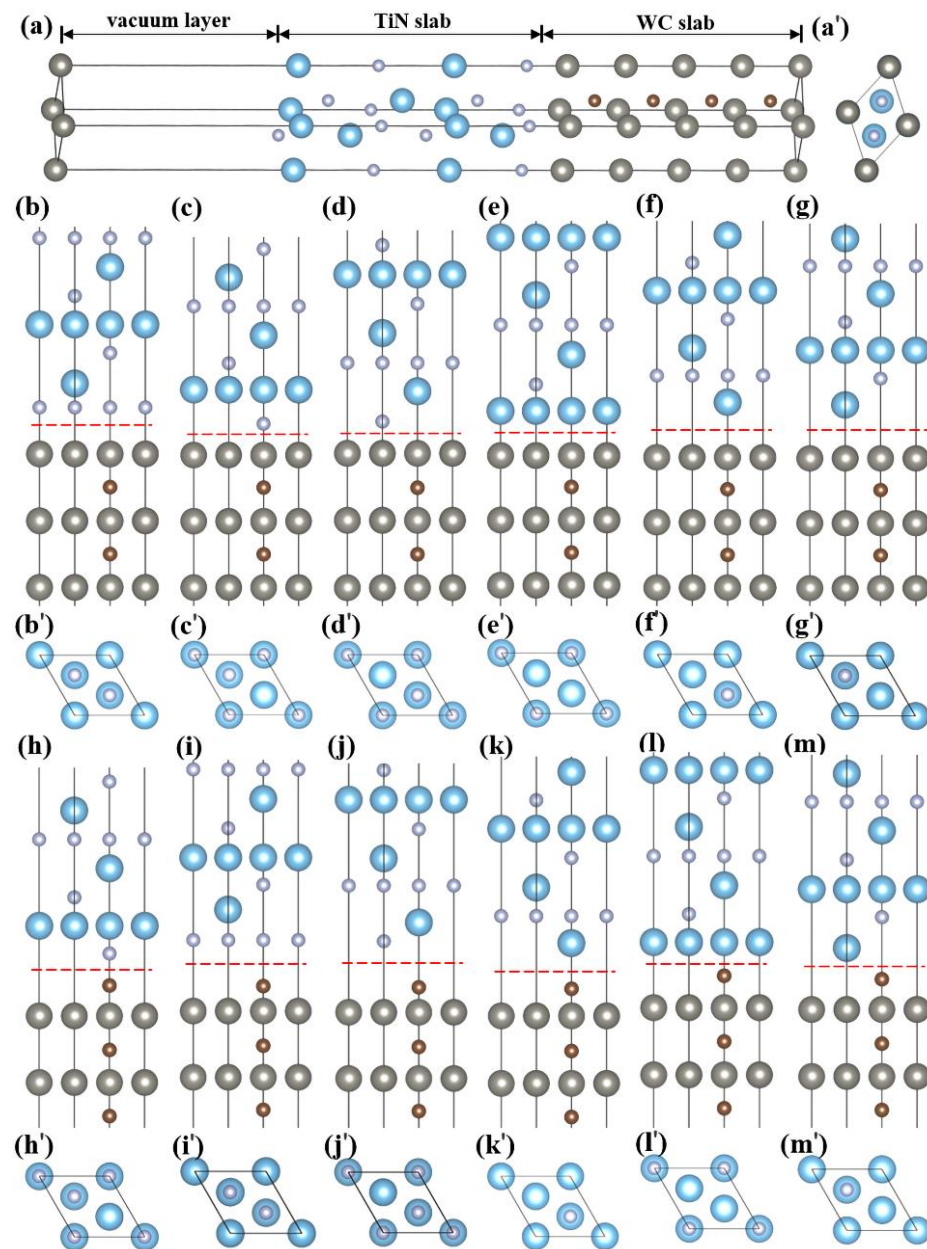


Figure 8. Interface models. (a) Complete computational model of the WC(0001)/TiN(111), (a') side view of model (a), (b) W-OT-N, (c) W-HCP-N, (d) W-Hole-N, (e) W-OT-Ti, (f) W-HCP-Ti, (g) W-Hole-Ti, (h) C-OT-N, (i) C-HCP-N, (j) C-Hole-N, (k) C-OT-Ti, (l) C-HCP-Ti, (m) C-Hole-Ti, and (b'~m') top views of the interface models, respectively.

3.4.2. Work of Adhesion and Interfacial Energy

The bond strength and stability of interface were assessed by interfacial adhesion work (W_{ad}) and interfacial energy (γ). The larger the W_{ad} , the stronger the bonding of the interface atoms. The following equation can be used to calculate the W_{ad} [34]:

$$W_{ad(WC/TiN)} = \frac{E_{WC} + E_{TiN} - E_{WC/TiN}}{A} \quad (13)$$

where A is the interface area, $E_{WC(0001)}$ and $E_{TiN(111)}$ are the total energy of WC(0001) slab and TiN(111) slab, respectively; $E_{WC/TiN}$ is the total energy of the interface of WC(0001)/TiN(111).

The following formula can be used to obtain the γ [34]:

$$\gamma_{(WC/TiN)} = \sigma_{WC} + \sigma_{TiN} - W_{ad} \quad (14)$$

where and σ_{TiN} are the surface energy of WC(0001) surface and TiN(111) surface respectively.

C-(HCP, Hole, OT)-N interface atoms were reconstructed during geometric optimization of the relaxed structure, and the geometric optimization did not converge, indicating that the interface between the WC(0001) C-terminated surface and the TiN(111) N-terminated surface was unstable. The relation curves of interfacial distance (d_0)- W_{ad} and d_0 - γ of different interfaces are shown in Figure 9. As can be seen, the termination type, stacking mode, and interfacial spacing of the interface structure have a direct effect on W_{ad} and γ . The listed nine interfacial structures all converge to a certain interfacial spacing, in which W_{ad} is the largest and γ is the smallest. This indicates that the interface structure converges to a relatively stable state at the corresponding extreme value of the curve. Table 6 summarizes the optimal W_{ad} , γ and d_0 for the relaxed geometry of the nine interfaces. It is obvious that, among the three types of interface structures, the stacking form has a significant impact on the W_{ad} , with all three types of interface structures demonstrating the relationship of HCP > Hole > OT. The interfacial HCP stacking form is the most powerful for bonding, as it can maintain the continuity of the ABAB... stacking mode of the WC bulk, and a similar effect is also observed in Al/WC [35], Fe/WC [36]. In the same interfacial structure, the HCP stacking form also has a smaller interfacial distance. In the same interfacial structure, the HCP stacking form also has a smaller interfacial distance, which is also beneficial to the interatomic interaction. Compared with the interface formed by the W-terminated to Ti-terminated, the interface structure formed by the C-terminated to Ti-terminated and the W-terminated to the N-terminated have a smaller d_0 . This is related to atomic radii and interactions between atoms. W belongs to the sixth period, and Ti belongs to the fourth period element. Both have larger atomic radii than the second period element C/N. The ordering relationship of W_{ad} for different interface structures is as follows: $W_{ad}(C-HCP-Ti) > W_{ad}(C-Hole-Ti) > W_{ad}(C-OT-Ti) > W_{ad}(W-HCP-N) > W_{ad}(W-HCP-Ti) > W_{ad}(W-Hole-Ti) > W_{ad}(W-Hole-N) > W_{ad}(W-OT-Ti) > W_{ad}(W-OT-N)$. The bonding strength of the C-Hole-Ti interface is the strongest ($W_{ad} = 8.899 \text{ J/m}^2$) among them. The large electronegativity difference between C and Ti results in a strong interaction between the two atoms. The ordering relationship of γ for different interface structures is as follows: $\gamma(C-HCP-Ti) < \gamma(C-Hole-Ti) < \gamma(W-HCP-Ti) < \gamma(W-Hole-Ti) < \gamma(W-OT-Ti) < \gamma(C-OT-Ti) < \gamma(W-HCP-N) < \gamma(W-Hole-N) < \gamma(W-OT-N)$. The stability of the C/Ti interface can be found to be greater than the stability of the W/N and W/Ti interfaces, while the γ of the C-HCP-Ti and C-Hole-Ti interfaces is less than zero, showing that they are thermodynamically stable [27]. The C-HCP-Ti interface is the most stable one with the smallest γ (-1.127 J/m^2).

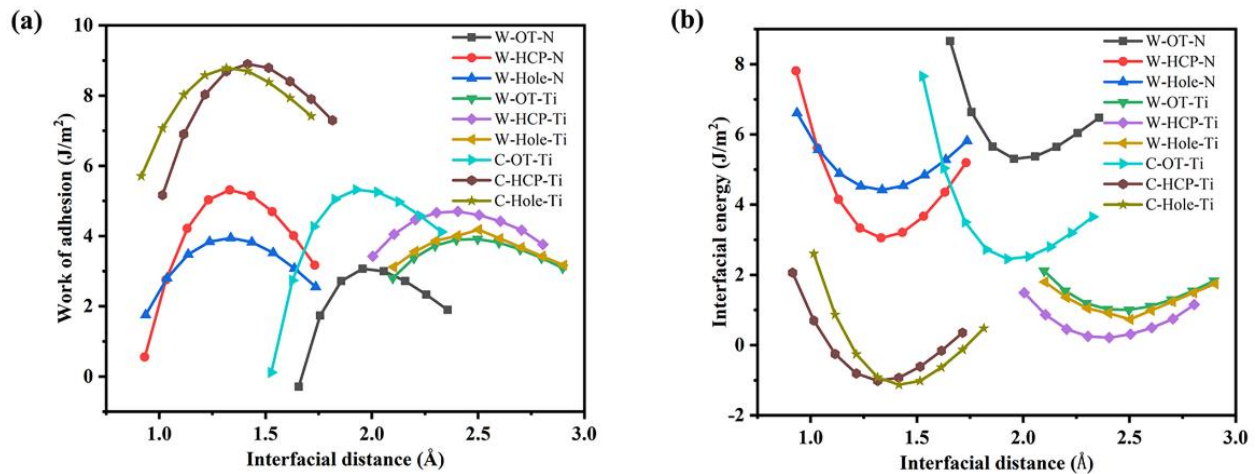


Figure 9. The relation curves of (a) d_0 - W_{ad} and (b) d_0 - γ of different interface models.

Table 6. Interface ideal W_{ad} , γ and d_0 for the nine WC(0001)/TiN(111) interface structure.

Termination		Stacking	Relaxed		
WC(0001)	TiN(111)		W_{ad} (J/m ²)	γ (J/m ²)	d_0 (Å)
W	N	OT	3.064	5.305	1.957
		HCP	5.313	3.051	1.332
		Hole	3.945	4.419	1.336
W	Ti	OT	3.914	1.004	2.498
		HCP	4.700	0.214	2.405
		Hole	4.183	0.734	2.503
C	Ti	OT	5.318	2.455	1.927
		HCP	8.899	−1.127	1.415
		Hole	8.786	−1.017	1.315

3.4.3. Interface Electronic Structure

The mechanical characteristics of the interface are determined by the atomic bonding strength [37]. Therefore, methods such as charge density difference and DOS are used to study the electronic structure of the WC(0001)/TiN(111) interface. The charge accumulation area and charge depletion area can be identified using the charge density difference to evaluate the transfer of interatomic charge [38]. Equation (15) can be used to compute the charge density difference [39]:

$$\rho_d = \rho_{total} - \rho_{WC} - \rho_{TiN} \tag{15}$$

where ρ_{total} is the total charge density of the WC(0001)/TiN(111) interface system; ρ_{WC} and ρ_{TiN} are the charge density of the WC and TiN slabs in the interface model.

The electronic structures of the C-HCP-Ti, W-HCP-N, and W-Hole-Ti interfaces were computed in order to better examine the properties of the interfaces. Figure 10 depicts the charge density difference at the interfaces of C-HCP-Ti, W-HCP-N, and W-Hole-Ti. According to the difference in charge distribution of atoms at different depths on both sides of the interface, it can be seen that the heterointerface structure affects the charge distribution of about two atomic layers on both sides of the interface, respectively. In Figure 10a, a charge depletion zone exists around the interface Ti atoms, and its distribution shape is different from that of the inner layer due to the influence of the interface atoms. An asymmetric charge accumulation region is around the C atom, its electron distribution

biased towards the Ti atoms, which indicates that the outer electrons of the Ti atoms are transferred to the C atoms during the interfacial bonding process. and its electron distribution is biased towards the adjacent Ti atoms, indicating that during the bonding process at the interface, the outer electrons from the Ti atoms are transferred to the C atoms. Due to the influence of the interface, the charge distribution of C atoms at the interface is different from that of the inner C atoms. The strong interaction between the C and Ti atoms at the interface is a sign of chemical bond formation. The redistribution characteristics of the interface charges prove that there are certain ionic characteristics between C and Ti atoms in addition to covalent bonds [20]. In Figure 10b, compared with the inner W atoms, there is an enlarged charge depletion region around the W atoms at the interface, and a charge accumulation region with electron distribution biased toward the adjacent W atom around the N atom at the interface, which indicates that during the bonding process at the interface, the outer electrons from the W atoms are transferred to the N atoms. The interaction between the W and N atoms indicates the formation of chemical bond. The W atoms at the interface have different charge distribution characteristics from the aforementioned two interface configurations, as can be seen in Figure 10c. The W atoms at this interface structure have a smaller charge depletion region than the inner W atoms, while the Ti atoms at the interface have an enlarged charge depletion region. There is a charge-sharing region between the interface W and Ti atoms, which indicates that the outer electrons of the W and Ti atoms are jointly transferred to the middle region of the interface to form a metallic bond. Additionally, the charge-sharing region is more inclined to the side of W atoms, which is related to the fact that W atoms have greater electronegativity than Ti atoms. Comparing the degree of charge transfer/aggregation of these three interface structures, it can be found that the interface atoms have different strengths of interaction: C-HCP-Ti>W-HCP-N>W-Hole-Ti, which is compatible with the calculation results of the interfacial bond strength presented above.

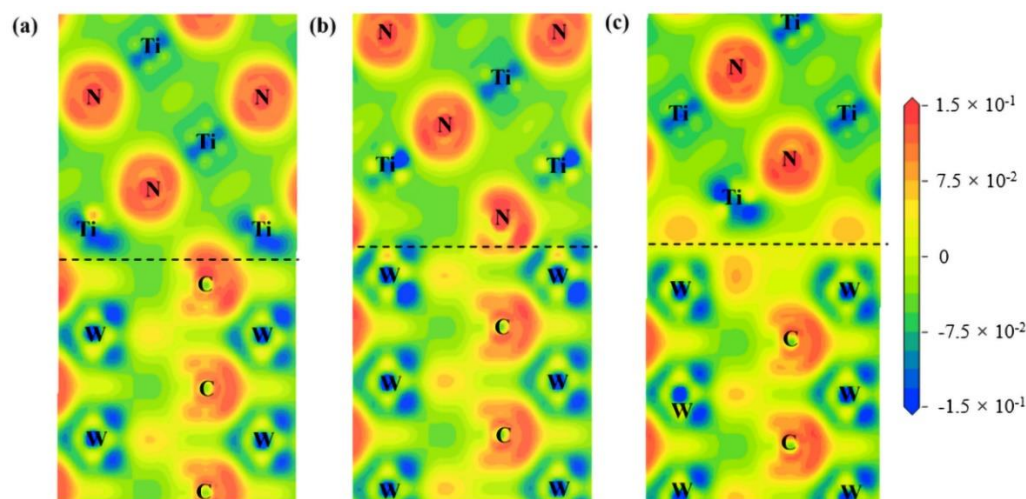


Figure 10. Charge density difference of the (1120) slice of WC(0001)/TiN(111) interfaces. (a) C-HCP-Ti, (b) W-HCP-N, (c) W-Hole-Ti.

Figure 11 depicts the PDOS of the C-HCP-Ti, W-HCP-N, and W-Hole-Ti interfaces. The DOS of the sub-interface atoms is very comparable to that of the inner atoms, while that of the interfacial atoms differs dramatically from that of the atoms in the inside structure. These differences represent the local charge redistribution features of the interfaces. All three interface structures contain Fermi level peaks, indicating that they have conductor-like properties. From -4.0 to -1.0 eV in Figure 11a, the peak morphologies and peak intensities of the C and Ti atoms are essentially the same, and there is clear orbital hybridization between them, demonstrating the formation of a potent covalent bond between the two atoms. The PDOS of C-atoms is much stronger than that of Ti-atoms between -8.0 eV

and 11.0 eV, indicating that the charge buildup was diverted to C-atoms and an ionic bond formed between them. As a result, the C-Hole-Ti interface's chemical bonds are a combination of ionic and covalent bonds. In Figure 11b, from -8.75 eV to -3.80 eV, the orbits of W-atoms and N-atoms both exhibit some degree of orbital hybridization, which affects the covalent bond that results from their interaction. From -15.0 eV to -17.5 eV, the fact that the PDOS of the N atom is significantly stronger than that of the W atom suggests that the charge buildup is diverted to the N atom, resulting in the formation of the ionic bond. Thus, the W-HCP-N interface forms ionic and covalent bonds. In Figure 11c, there is no orbital hybridization effect between the orbitals of W and Ti atoms at the interface, indicating that there is no interaction between them and no covalent bond is formed, which may be related to the larger interface distance (2.503 Å). Both W atoms and Ti atoms have a large number of electronic states close to the Fermi level, indicating the formation of strong metallic bonds. Therefore, the W-HCP-Ti interface is the interaction of metallic bonds.

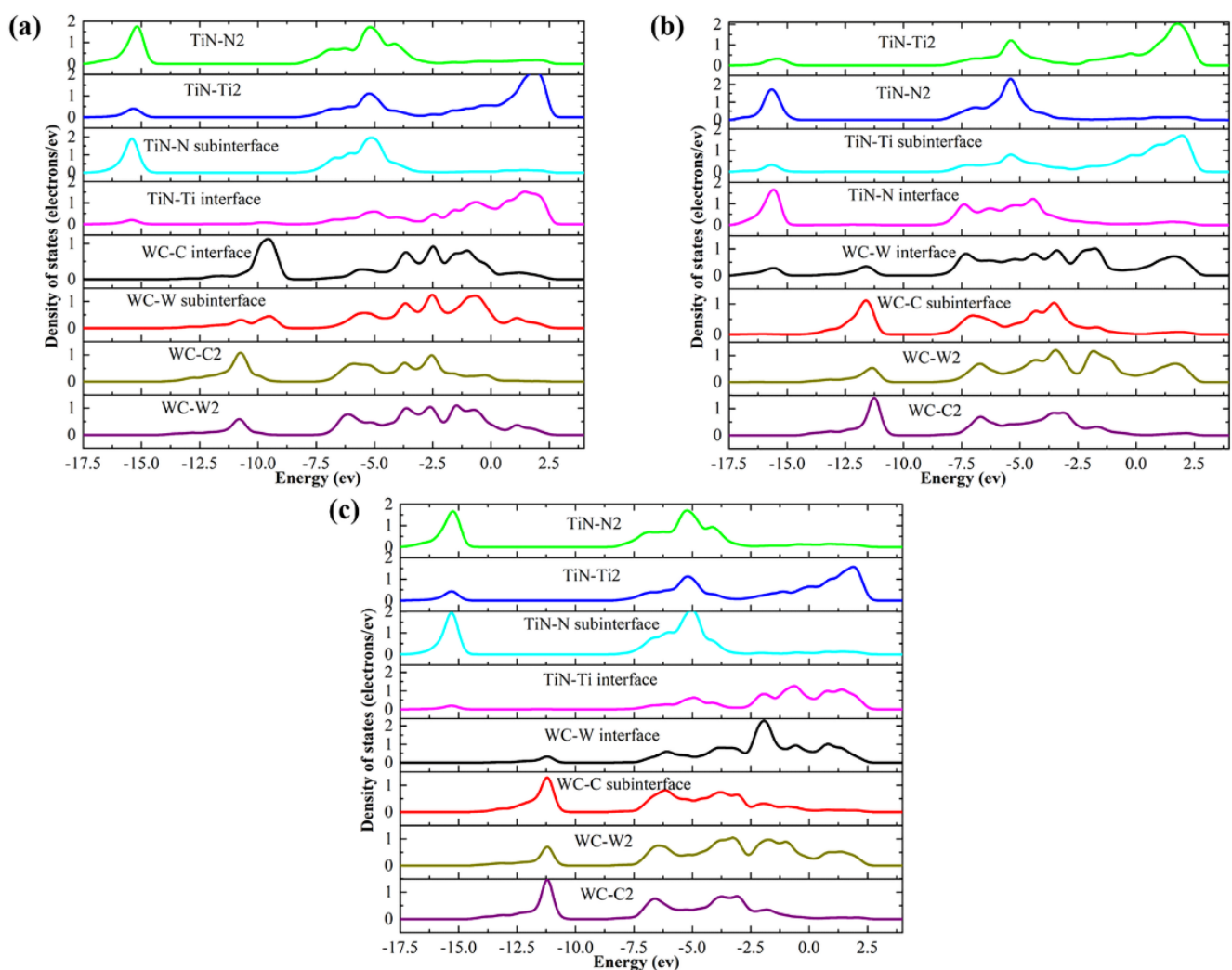


Figure 11. Partial DOS for WC/TiN interfaces: (a) C-HCP-Ti, (b) W-HCP-N, (c) W-Hole-Ti.

4. Conclusions

This work is based on the application background of TiN coating widely used as a wear-resistant layer and adhesive layer in the field of cemented carbide-coated tools to improve the bonding performance of the film-substrate interface. The interfacial properties between the WC substrate and TiN coating were investigated by using first-principles calculations. The polar WC(0001)/TiN(111) interface with the minimum lattice mismatch was chosen in accordance with the lattice mismatch theory. Twelve interface models were

built in accordance with the atomic termination types and atomic stacking forms, but only nine interface models were explored due to the non-convergence of the geometric optimization of the C-(OT, HCP, Hole)-N interface model. The analysis of adhesion work, interfacial energy, electronic structure, etc., aims to reveal the bonding strength, stability and bonding mechanism of different termination state interface types. The conclusions are as follows:

1. The chemical bonds of the WC bulk are a mixture of metal, ionic, and covalent bonds; the anisotropy of the elastic properties of WC bulk is mainly contributed by the z direction, and there is no anisotropy in the x/y direction. The chemical bond of TiN bulk is a mixture of metal and polar covalent bonds; the elastic properties of TiN bulk have strong anisotropy and high symmetry. The symmetry of elastic properties is related to the symmetry of its crystal structure.
2. The lattice mismatch ratio of WC(0001) and TiN(111) slabs is 2.7%, indicating that WC(0001) and TiN(111) can perform good lattice matching.
3. The interfacial atomic stacking form of HCP has a larger W_{ad} compared with other stacking forms due to the preservation of the continuity of the WC structure. Among the nine interface models, the maximum W_{ad} of the C-HCP-Ti interface is 8.899 J/m^2 , and the separation distance is 1.415 \AA , indicating that the bonding strength of C-HCP-Ti is the strongest, which is consistent with the strong interaction of electrons between C/Ti atoms at the interface.
4. The γ values of the C-HCP-Ti, C-Hole-Ti interfaces are less than zero, indicating that they are thermodynamically stable. The C-HCP-Ti structure, the most stable interface structure with the smallest γ value (-1.127 J/m^2), forms covalent and ionic bonds at the interface.

This study offers a crucial theoretical framework for understanding the formation mechanism of the film–substrate interface of cemented carbide-coated tools.

Author Contributions: Conceptualization, M.W., Y.L. and L.W.; methodology, M.W. and L.W.; software, M.W. and D.H.; formal analysis, L.W.; investigation, M.W. and D.H.; data curation, M.W.; writing—original draft preparation, M.W.; writing—review and editing, Y.L., H.C. and D.H.; visualization, L.W.; supervision, H.C.; project administration, Y.L. All authors have read and agreed to the published version of the manuscript.

Funding: This research was funded by the Sichuan Science and Technology Program (2021YJ0004).

Institutional Review Board Statement: Not applicable.

Informed Consent Statement: Not applicable.

Data Availability Statement: The data created in this study are fully depicted in the article.

Conflicts of Interest: The authors declare no conflict of interest.

References

1. Garcia, J.; Cipres, V.C.; Blomqvist, A.; Kaplan, B. Cemented carbide microstructures: A review. *Int. J. Refract. Met. Hard Mater.* **2019**, *80*, 40–68. [[CrossRef](#)]
2. Wang, K.-F.; Tang, X.-L.; Jiao, S.; Chou, K.-C.; Zhang, G.-H. A short and facile process to synthesize WC-Co cemented carbides. *Int. J. Refract. Met. Hard Mater.* **2020**, *92*, 105288. [[CrossRef](#)]
3. Montenegro, P.; Gomes, J.; Rego, R.; Borille, A. Potential of niobium carbide application as the hard phase in cutting tool substrate. *Int. J. Refract. Met. Hard Mater.* **2018**, *70*, 116–123. [[CrossRef](#)]
4. Xie, H.; Liu, Y.; Ye, J.; Li, M.; Zhu, Y.; Fan, H. Effect of $(\text{Cr}_{0.8}\text{V}_{0.2})_2(\text{C},\text{N})$ addition on microstructure and mechanical properties of WC-8Co cemented carbides. *Int. J. Refract. Met. Hard Mater.* **2014**, *47*, 145–149. [[CrossRef](#)]
5. Wang, B.; Wang, Z.; Yin, Z.; Yuan, J.; Jia, J. Preparation and properties of the VC/Cr₃C₂/TaC doped ultrafine WC-Co tool material by spark plasma sintering. *J. Alloys Compd.* **2020**, *816*, 152598. [[CrossRef](#)]
6. Schalk, N.; Tkadletz, M.; Mitterer, C. Hard coatings for cutting applications: Physical vs. chemical vapor deposition and future challenges for the coatings community. *Surf. Coat. Technol.* **2022**, *429*, 127949. [[CrossRef](#)]
7. Boing, D.; de Oliveira, A.J.; Schroeter, R.B. Limiting conditions for application of PVD (TiAlN) and CVD (TiCN/Al₂O₃/TiN) coated cemented carbide grades in the turning of hardened steels. *Wear* **2018**, *416–417*, 54–61. [[CrossRef](#)]

8. Chim, Y.C.; Ding, X.Z.; Zeng, X.T.; Zhang, S. Oxidation resistance of TiN, CrN, TiAlN and CrAlN coatings deposited by lateral rotating cathode arc. *Thin Solid Film.* **2009**, *517*, 4845–4849. [[CrossRef](#)]
9. Derflinger, V.H.; Schütze, A.; Ante, M. Mechanical and structural properties of various alloyed TiAlN-based hard coatings. *Surf. Coat. Technol.* **2006**, *200*, 4693–4700. [[CrossRef](#)]
10. Huang, M.; Chen, Z.; Wang, M.; Li, Y.; Wang, Y. Microstructure and properties of TiCrN coatings by arc ion plating. *Surf. Eng.* **2016**, *32*, 284–288. [[CrossRef](#)]
11. Weicheng, K.; Hui, S.; Dejun, K. Microstructure and Tribological Properties of Cathodic Arc Ion Plated TiAlN and TiSiN Coatings at High Temperatures. *J. Tribol.* **2018**, *140*, 041301. [[CrossRef](#)]
12. Chen, T.; Xie, Z.; Gong, F.; Luo, Z.; Yang, Z. Correlation between microstructure evolution and high temperature properties of TiAlSiN hard coatings with different Si and Al content. *Appl. Surf. Sci.* **2014**, *314*, 735–745. [[CrossRef](#)]
13. Chang, Y.-Y.; Cai, M.-C. Mechanical property and tribological performance of AlTiSiN and AlTiBN hard coatings using ternary alloy targets. *Surf. Coat. Technol.* **2019**, *374*, 1120–1127. [[CrossRef](#)]
14. Zhong, Z.-q.; Zhang, L.; Chen, Y.; Gu, J.-h.; Zhu, J.-f.; Xiong, X.-j. Strategy for achieving high-performance PVD nano-multilayered AlTiN/TiN coated milling tool: Fine platelet-grained WC–Co substrate and interface regulation. *Surf. Coat. Technol.* **2022**, *435*, 128265. [[CrossRef](#)]
15. Zhong, Z.-Q.; Zhang, L.; Zhou, L.; Qiu, L.-C.; Shi, H.-D.; Yang, M.-L.; Zhu, J.-F. Cutting performances and the related characteristics of CVD coated hardmetal inserts changed by post-treatments. *Int. J. Refract. Met. Hard Mater.* **2018**, *70*, 162–168. [[CrossRef](#)]
16. Ghailane, A.; Larhlimi, H.; Tamraoui, Y.; Makha, M.; Busch, H.; Fischer, C.B.; Alami, J. The effect of magnetic field configuration on structural and mechanical properties of TiN coatings deposited by HiPIMS and dcMS. *Surf. Coat. Technol.* **2020**, *404*, 126572. [[CrossRef](#)]
17. Bouzakis, K.D.; Skordaris, G.; Michailidis, N.; Asimakopoulos, A.; Erkens, G. Effect on PVD coated cemented carbide inserts cutting performance of micro-blasting and lapping of their substrates. *Surf. Coat. Technol.* **2005**, *200*, 128–132. [[CrossRef](#)]
18. Skordaris, G.; Bouzakis, K.D.; Stergioudi, F.; Kouparanis, S.; Boumpakis, A.; Bouzakis, A. Cutting performance improvement of MTCVD coated cemented carbide inserts via appropriate heat treatment. *CIRP Ann.* **2020**, *69*, 45–48. [[CrossRef](#)]
19. Martinez, J.; Sinnott, S.B.; Phillpot, S.R. Adhesion and diffusion at TiN/TiO₂ interfaces: A first principles study. *Comput. Mater. Sci.* **2017**, *130*, 249–256. [[CrossRef](#)]
20. Zhao, X.; Zhuo, Y.; Liu, S.; Zhou, Y.; Zhao, C.; Wang, C.; Yang, Q. Investigation on WC/TiC interface relationship in wear-resistant coating by first-principles. *Surf. Coat. Technol.* **2016**, *305*, 200–207. [[CrossRef](#)]
21. Zavodinsky, V.G.; Kabaldin, Y.G. Modeling study of adhesion in the TiN/Ti, TiN/ZrN, TiN/Ti/ZrN, and TiN/Zr/ZrN layered systems. *J. Adhes.* **2020**, *96*, 633–646. [[CrossRef](#)]
22. Rao, L.; Liu, H.; Shao, W.; Hu, T.; Xing, X.; Ren, X.; Zhou, Y.; Yang, Q. Investigation on the interface characteristic between TiN and diamond by first-principles calculation. *Diam. Relat. Mater.* **2020**, *109*, 108023. [[CrossRef](#)]
23. Fan, X.; Chen, B.; Zhang, M.; Li, D.; Liu, Z.; Xiao, C. First-principles calculations on bonding characteristic and electronic property of TiC(111)/TiN(111) interface. *Mater. Des.* **2016**, *112*, 282–289. [[CrossRef](#)]
24. Alves, S.M.; Albano, W.; de Oliveira, A.J. Improvement of coating adhesion on cemented carbide tools by plasma etching. *J. Braz. Soc. Mech. Sci. Eng.* **2017**, *39*, 845–856. [[CrossRef](#)]
25. Yang, G.; Liu, Y.; Hang, Z.; Xi, N.; Fu, H.; Chen, H. Adhesion at cerium doped metal-ceramic α -Fe/WC interface: A first-principles calculation. *J. Rare Earths* **2019**, *37*, 773–780. [[CrossRef](#)]
26. Li, J.; Yang, Y.; Feng, G.; Luo, X.; Sun, Q.; Jin, N. Adhesion and fracture toughness at α -Ti(0001)/TiC(111): A first-principles investigation. *Appl. Surf. Sci.* **2013**, *286*, 240–248. [[CrossRef](#)]
27. Rao, L.; Liu, H.; Liu, S.; Shi, Z.; Ren, X.; Zhou, Y.; Yang, Q. Interface relationship between TiN and Ti substrate by first-principles calculation. *Comput. Mater. Sci.* **2018**, *155*, 36–47. [[CrossRef](#)]
28. Gaillac, R.; Pullumbi, P.; Coudert, F.-X. ELATE: An open-source online application for analysis and visualization of elastic tensors. *J. Phys. Condens. Matter.* **2016**, *28*, 275201. [[CrossRef](#)] [[PubMed](#)]
29. Zhang, J.; Sides, S.; Bates, F.S. Ordering of Sphere Forming SISO Tetrablock Terpolymers on a Simple Hexagonal Lattice. *Macromolecules* **2012**, *45*, 256–265. [[CrossRef](#)]
30. Setyawan, W.; Curtarolo, S. High-throughput electronic band structure calculations: Challenges and tools. *Comput. Mater. Sci.* **2010**, *49*, 299–312. [[CrossRef](#)]
31. Bachurin, D.V.; Weygand, D.; Gumbsch, P. Dislocation–grain boundary interaction in $\langle 111 \rangle$ textured thin metal films. *Acta Mater.* **2010**, *58*, 5232–5241. [[CrossRef](#)]
32. Bramfitt, B.L. The effect of carbide and nitride additions on the heterogeneous nucleation behavior of liquid iron. *Metall. Trans.* **1970**, *1*, 1987–1995. [[CrossRef](#)]
33. Boettger, J. Nonconvergence of surface energies obtained from thin-film calculations. *Phys. Rev. B Condens. Matter.* **1994**, *49*, 16798–16800. [[CrossRef](#)] [[PubMed](#)]
34. Xian, Y.; Qiu, R.; Wang, X.; Zhang, P. Interfacial properties and electron structure of Al/B₄C interface: A first-principles study. *J. Nucl. Mater.* **2016**, *478*, 227–235. [[CrossRef](#)]
35. Siegel, D.J.; Hector, L.G.; Adams, J.B. Adhesion, stability, and bonding at metal/metal-carbide interfaces: Al/WC. *Surf. Sci.* **2002**, *498*, 321–336. [[CrossRef](#)]

36. Li, Y.; Gao, Y.; Xiao, B.; Min, T.; Ma, S.; Yi, D. Theoretical calculations on the adhesion, stability, electronic structure, and bonding of Fe/WC interface. *Appl. Surf. Sci.* **2011**, *257*, 5671–5678. [[CrossRef](#)]
37. Xue, H.; Wei, X.; Guo, W.; Zhang, X. Bonding mechanism study of active Ti element and α -Al₂O₃ by using first-principle calculation. *J. Alloys Compd.* **2020**, *820*, 153070. [[CrossRef](#)]
38. Shi, Z.; Liu, S.; Zhou, Y.; Xing, X.; Ren, X.; Yang, Q. Structure and properties of YAlO₃/NbC heterogeneous nucleation interface: First principles calculation and experimental research. *J. Alloys Compd.* **2019**, *773*, 264–276. [[CrossRef](#)]
39. Fiorentini, V.; Methfessel, M. Extracting convergent surface energies from slab calculations. *J. Phys. Condens. Matter.* **1996**, *8*, 6525–6529. [[CrossRef](#)]